

# **Earthquake behavior of the San Andreas and San Jacinto Faults with Structure from Motion topography (SCEC award #13084)**

Edwin Nissen (Colorado School of Mines), J Ramon Arrowsmith, Srikanth Saripalli (Arizona State University), Kate Scharer (US Geological Survey, Pasadena)

## **1. Summary of major research findings**

The project aims are (1) to detect and image offsets along southern California faults using improved, decimeter-resolution topography generated with Structure from Motion (SfM), providing additional slip data in areas where airborne LiDAR has been unable to reveal offsets; (2) to investigate the shapes of these channels with scarp degradation models to try to date channel abandonment (and constrain offset age) directly from the topography; and (3) to test a range of different unmanned platforms and develop improved means of stripping vegetation from and geo-referencing the resulting point clouds. The project builds on a previous SCEC award in which we explored SfM topographic mapping using remote controlled helicopters.

Initial research findings were submitted for publication in *Geosphere* in December 2013. This PhD student-led paper comprised a full documentation of the equipment and set-up needed for SfM topographic mapping, and comparisons between the resultant SfM point clouds and DEMs with those derived from more traditional laser-based mapping. Our major findings are summarized below:

- We document a simple, affordable SfM workflow – based upon an unmanned helium balloon or motorized glider, a cheap camera, and semi-automated software - which generates topography and coregistered texture (color) of areas with sparse or low-lying vegetation.
- We illustrate the technique at two sites on southern California faults covered by existing airborne or terrestrial LiDAR. At the first site, a ~0.1 km<sup>2</sup> catchment on the San Andreas fault, a ~720 points/m<sup>2</sup> point cloud and 3 cm digital elevation model (DEM) were produced from 233 photos collected ~50 m above ground level (AGL). When a few GPS ground control points are incorporated, closest point vertical distances to the much sparser (~4 points/m<sup>2</sup>) airborne LiDAR point cloud are mostly <3 cm.
- The second site spans a ~1 km section of the 1992 Landers earthquake scarp. A ~130 points/m<sup>2</sup> point cloud and 2 cm DEM were produced from 450 photos taken from ~60 m above ground level (AGL). Closest point vertical distances to overlapping terrestrial LiDAR data of comparable density are mostly <6 cm. Each SfM survey took just ~2 hours to complete and several hours to generate the scene topography and texture.

Additional fieldwork in 2013 focused on two main areas: (a) the Banning and Mission Creek strands of the San Andreas fault, the relative activities of which remain controversial; and (b) the El Mayor Cucapah earthquake rupture, where we have integrated our SfM data into efforts to characterize scarp degradation using multi-temporal terrestrial LiDAR mapping. Analyses of these datasets are ongoing, and results are not yet ready for presentation in this report.

## 2. Technical description

### 2.1 Workflow for generating high-resolution topography with SfM

Below, we discuss our choice of platform and strategy for photograph collection and our preferred way of processing this imagery and generating topography. A key goal of ours is to find an appropriate balance between the affordability and accessibility of the system (its cost, ease and speed of use) and the quality of the resulting topographic data (its accuracy and density). As a result, our methodology differs somewhat from the procedures followed in the SfM studies described previously (Fig. 1). In particular, we designed our approach to be easily completed by a person working alone, or in situations where data collection and processing must be expedited, such as field mapping after an earthquake.

We chose to use both a radio-controlled motorized glider and a tethered helium balloon as camera platforms, both being easily deployed and affordable, costing a few hundred dollars in total. The **motorized glider** can cover larger areas more quickly, but requires more experience to control remotely; on the other hand, a skilled pilot has more control over the platform position and camera angle. Like many other UAVs, the kite also has the potential to be programmed to fly along a preset route that requires little interference by the operator. Our glider was purchased as a kit from Electric Flights and assembled in a few hours. After hand launching, the glider is operated using a 2.4 GHz Spektrum DX6i Transmitter and Spektrum 6100e Park Receiver and powered with a single 3000 mAh 4 Cell 14.8V Lithium Polymer battery, giving a flight time of around 20 minutes. The glider carries a lightweight Canon PowerShot SX230 HS camera, which has a 5 mm focal length and internal GPS. Interval shooting can be triggered at a specified delay time by programming the SD card with the freely available Canon Hack Development Kit (CHDK). The **helium balloon** offers the advantage of simplicity, as a single person can pull the tethered platform across the target area from the ground. Our balloon inflates to  $\sim 4 \text{ m}^3$  and carries a harness (a Brooxes picavet) from which we attached a downward-pointing Nikon D5100 camera with an 11 mm Toshiba lens and a connected Easytag GPS tagger. The weight of the camera, lens, and GPS tagger totals  $\sim 1 \text{ kg}$ . The balloon is tethered using a lightweight kite string and reel. The camera is set to interval shooting mode and the delay between shots is specified. We also set the focus to infinity and choose an appropriate (fixed) exposure setting depending on light conditions.

The strategy for photograph collection depends on the shape and size of the target area, as well as the desired resolution of the topographic data. We find that a single pass of the balloon or glider is sufficient to capture small-scale topography along thin, sublinear targets, whilst “lawnmower” acquisition patterns effectively cover wider targets. Given sufficient photograph overlap, data resolution is determined by the height of the platform. In our case, the length and weight of our kite string limited the balloon to an elevation of  $\sim 120 \text{ m}$  AGL (at close to sea level), while the glider can fly at a few hundred meters AGL. When photographs are taken closer to the ground, SfM point cloud density and DEM resolution improves at the expense of smaller photograph footprint size and overlap, with a resulting increase in the time taken to survey a given area.

We build the SfM point clouds and DEMs using the commercial Photoscan Pro software made by Agisoft LLC, from now on termed Photoscan. We choose this software for its two principle advantages over

other published procedures (Fig. 1). Firstly, Photoscan is able to implement camera GPS positions into the SfM calculations as opposed to relying entirely on ground control points (GCPs) for scene georeferencing, as the other workflows do. Using these initial position estimates also speeds up the scene reconstruction. Secondly, Photoscan can do all of the steps in the processing chain itself, whereas the other approaches rely on several separate programs to build a final, georeferenced model (Fig. 1).

Next, we briefly describe the processing steps involved in generating topography and texture from a photoset. The highly-automated Photoscan workflow consists of four main steps. (1) The photographs are loaded, including their tagged GPS positions if available. Usually, these are stored in the EXIF metadata of each JPEG along with certain other camera parameters and are easily loaded into Photoscan. (2) Matching features are identified and the scene structure - camera positions and orientations and colored point cloud - is constructed. At this stage, the point cloud can be exported in ASCII or LAS formats and in a user specified coordinate system. (3) A DEM is constructed from the point cloud by fitting polygons to points that characterize a face of the surface. This can also be exported in a variety of common formats and coordinate systems. (4) Finally, an orthorectified composite photograph is generated. Some guidance by the user is required. In step (1), we first quality check the photos, discarding those that are blurry or dominated by sky (this can occur during glider flights when the aircraft banks). Steps (2) and (3) are automated processes guided by user-specified accuracy and quality options. Step (2) can be completed at three levels of accuracy, which trade off against processing time. While still at the survey site, we run this step at the lowest setting on a field laptop in order to check that we have good photograph coverage, but for the final point clouds presented in this study we choose the highest level possible. At this point, Photoscan can interactively tidy up the point cloud by removing any points that have high reprojection or reconstruction errors or that lie far from the surface. This step is not required, but it does improve the point cloud by filtering erroneous points and leaving only those that represent a continuous surface; it can also make subsequent gridding much quicker.

Step (3) can be completed at five quality levels, with processing time again increasing significantly at each level of improvement. This step can also be further expedited by using alternative programs to generate the DEM, such as GEON points2grid, which computes at each grid node the minimum, maximum, mean, or inverse distance weighted mean value of points within a user-specified search radius. This requires more interaction from the user, but is less time intensive than step (3) in Photoscan and avoids certain artifacts. As the number of photos used to build the point cloud increases, the time required to complete these steps grows significantly. When using low quality settings on tens of photos, Photoscan can complete the workflow in minutes, while high quality settings on hundreds of photos can take multiple days. Processing time is expedited by using a powerful computer with a large RAM, multiple cores, and a high quality graphics card. Here, we use an eight-core Intel 7 processor with 32 GB Ram and an Nvidia GeForce 670 graphics card. A few additional steps are required to register the grids if very accurate geospatial coordinates are desired. As described above, the SfM data are initially georeferenced using the instantaneous coordinates of the camera's GPS that are stamped to the metadata of each picture. This capability significantly decreases the processing time as an automated part of the photo alignment stage, and eliminates the time spent deploying and/or identifying ground control points. However, small errors in the camera GPS location can lead to shifting, tilting, or warping

of the resulting topographic data.. For SfM applications in which relative precision of the elevation values throughout a scene is crucial, the user must incorporate independently-located ground control points. In this case, the user assigns coordinates to a few evenly distributed features within the scene, and Photoscan optimizes the point cloud to better fit these new constraints. In the data presented below, we use ground control points deployed and surveyed using differential GPS.

## **2.1 Example dataset: the Washington St site, Palm Springs**

The Washington Street site covers a small section of the southern Banning strand of the San Andreas Fault, along the southwestern margin of the Indio Hills due east of Palm Springs, California. Neither this fault, nor the northern Mission Creek strand, have ruptured historically, contributing to the uncertainty in how the slip is partitioned between these two sub-parallel structures. At the target site, the Banning fault strand crosses a sparsely vegetated Quaternary alluvial fan incised by an active channel.

We collected over 1000 photographs of the Washington Street site covering a  $\sim 300 \times \sim 300$  m area ( $\sim 0.1$  km<sup>2</sup>) using both the helium balloon and motorized glider as camera platforms. Data collection, including platform assembly and disassembly of both the balloon and glider, took less than 2 two hours. We selected  $\sim 800$  usable photos captured from the balloon at three different heights AGL: 50 m, 100 m, and  $\sim 120$  m. For each height, we pulled the balloon along a lawn-mower path where each line intersected the fault at a near-perpendicular angle. The Nikon D5100 camera shot interval was set to 5 s. In addition, we captured took 107 photos from the glider flying at heights of 150-300 m AGL, capturing photographs from a wide variety of elevations and viewing angles. The glider's Canon PowerShot SX230 HS camera was programmed to capture photographs at a 5 s interval.

Following photo collection and selection, we loaded and processed each set of photos independently in Photoscan, in order to compare results for different platform heights, collection strategies, and processing settings. For each balloon photoset, we initially built the DEMs at the medium quality setting, but for the higher glider photoset (up to 300 m AGL) we used high quality. Although increasing the height of the balloon enabled wider ground footprints of each photo (and therefore quicker coverage of the whole site), the resulting point cloud density suffered; for example, doubling the height of the balloon decreased the point cloud density by more than 50%. We also produced a DEM at the best available (ultra-high) quality setting for the low altitude balloon photoset to observe how this alters the resolution. Its 3 cm resolution is three times finer than that of the medium quality DEM constructed from the same photoset, but took considerably longer to build.

SfM results at the ultra-high quality setting are shown in Figure 2. At  $>700$  points/m<sup>2</sup>, the SfM point cloud is significantly denser than that of the airborne LiDAR. Furthermore, each point in the cloud is colored with its red/green/blue (RGB) values, an improvement upon airborne LiDAR in which only a return intensity is recorded. This color information could potentially be useful for stripping vegetation from the scene (in this case bushes, which appear as dark lumps contrasting with the lighter alluvium). Large scale views of the 3 cm-resolution SfM DEM and the B4 airborne LiDAR DEM gridded at 0.5 m resolution are shown in Fig. 2c and 2d, respectively. At this scale, the LiDAR DEM appears pixilated and in this locality it also suffers from a striped “corduroy” pattern, an artifact common to airborne LiDAR

data due to misaligned overlapping flight lines. The SfM DEM reveals cm-scale details – discussed below – which do not stand out in the airborne LiDAR DEM due to its poorer resolution and corduroy.

When the DEM is built at lower qualities, we find that Photoscan fits the point cloud surface with large, sharp polygons. Although the resolution of the DEM is nominally 10 cm, fine details of the geomorphology are badly obscured by these artifacts. This is an issue with the gridding of the DEM rather than with the point cloud itself, and alternative gridding software generated much better results using the same point cloud data. We used the free GEON points2grid package with a node spacing of 0.08 m and using the mean value from within a search radius of 0.10 m, and were able to visually eliminate much of the site's vegetation while still preserving most geomorphic detail.

***Assessing accuracy: no ground control points.*** Previous studies had mixed results when comparing SfM and lidar datasets. Here, we investigate how well aligned the SfM topography is before applying ground control points with the B4 airborne LiDAR dataset. Until now, our SfM datasets have been georeferenced using only the camera GPS points and lens metadata stamped to each JPEG. We use two steps to assess the accuracy of this dataset, both implemented in the open source software CloudCompare. (1) We apply the iterative closest point algorithm (ICP) to achieve a global alignment of the two point clouds. ICP works iteratively to find the rigid body transformation (translation and rotation) that minimizes closest point pair distances between clouds. This step helps account for remaining differences in the global registration of the two datasets that result from changes in absolute GPS positioning between the two surveys, but does not affect the internal shape of either dataset. In this instance, all translational components were on the scale of meters, reflecting a significant mismatch in the GPS registration of the two surveys. All rotational components were  $\sim 0.01$  radians, values that reflect a significant tilting of the SfM dataset. For some applications this is an important point, because without an alternative (LiDAR) dataset to register the SfM cloud to there would be residual errors in slope. (2) Having applied the ICP transformation, cloud-to-cloud distances can be measured independent of these registration differences and which therefore only reflect discrepancies in the internal shape of each point cloud. For each point in the LiDAR point cloud, we locate the nearest point in the transformed SfM cloud and measure the vertical component of the Euclidian distance between the two. We choose to measure this distance at each LiDAR point, rather than at each SfM point, based on the lower density of the LiDAR points; this configuration ensures smaller distances between each pair of compared points.

Results of this two-step comparison are as follows. Half of the LiDAR points deviate vertically from the closest SfM point by  $<10$  cm and 90% by  $<41$  cm. The largest deviations are observed in four types of areas: (1) steep slopes, (2) outer edges of the difference map, (3) large bushes, and (4) active or recently active stream channels. In the case of steep terrain (1), it is unclear whether the deviations result from errors in SfM point positioning, or from uncertainties in LiDAR heights which increase on steep slopes due to the larger footprint of the steeply inclined laser beam. Higher deviations around the outer edges of the difference map (2) are likely to be primarily caused by errors in SfM point positions, as these were reconstructed using fewer photographs from a smaller range of look angles than data in the central part of the scene. Bushes (3), many of which appear as red dots in the difference map, may have grown between the 2005 LiDAR survey and the 2013 SfM survey, and/or laser penetration through the bushes

make them appear smaller in the LiDAR, or these deviations may simply reflect differences in how the two techniques characterize vegetation. The stream channel (4) switched its primary course during the 8-year period between surveys (Figure 2c-d) such that both the old and new stream channels have undergone some erosion, which is reflected in the difference map. Despite the low cloud-to-cloud distance errors, the rotational components of the ICP alignment matrix determined in Cloud Compare (step 1, above) indicate that our SfM point cloud is tilted compared to the airborne LiDAR.

***Assessing accuracy with ground control points (GCPs).*** For some tectonic applications of high resolution topography, such as scarp degradation modeling and river profile analysis, these errors in slope could compromise the quantitative analysis of the landscape. We therefore investigate whether providing Photoscan with a few precisely located ground control points (GCPs) as additional constraints can eliminate tilting from the SfM topography.

First, we produced a modified SfM point cloud optimized in Photoscan using nine GCPs. These were sourced from a set of differential GPS transects, which follow several features within the central portion of the Washington Street site. The transects were collected with a Trimble GeoXH Handheld GPS in January 2013, and were post-processed with local base stations to produce absolute uncertainties of ~20 cm. The GPS data were overlain on an aerial photograph, which was easy to correlate with the SfM orthophoto. We identified features distinguishable in both images that corresponded to points on the GPS transect, and marked their locations (x, y and z UTM coordinates) in the SfM point cloud. We used these to illustrate how the SfM can be improved where no LiDAR exists. Next, we repeat the ICP and cloud-to-cloud differencing tests with this GCP-optimized SfM point cloud and the airborne LiDAR. The incorporated GCPs eliminate much of the apparent warping: 50% of the LiDAR points now deviate vertically from the closest SfM point by <3 cm and 90% by <13 cm (Figure 3). Crucially, these vertical residuals are close to the 5-10 cm spot height uncertainties reported for the B4 LiDAR survey. While small residuals are still present in areas of high slope, vegetation and around the SfM survey border, the switched stream channels now stand out indicating genuine morphological change.

### **3. Intellectual merit**

The intellectual merit is to improve characterization and age determination for geomorphic displacements – principally scarps and offset channels – using high-resolution topography data. This will help efforts to understand slip rates and earthquake potential of active faults across southern California. A unique aspect of the project compared to previous work on these topics is the use of SfM to generate topographic data of sufficient resolution and precision both cheaply and quickly.

### **4. Broader impacts**

Our findings have been presented at the 2013 SCEC and AGU meetings and are in review at *Geosphere*. Both presentations and the paper were led by a female Ph. D. student, Kendra Johnson. We have also been active in introducing and demonstrating SfM to the community, including at SCEC-sponsored workshops at the Earthquake Research Institute, University of Tokyo (September 2013) and the Supercomputer Center University of California, San Diego (November 2013), as well as at the recent UNAVCO Science Workshop (March 2014).

## **5. Bibliography**

### **Journal articles**

Johnson, K., Nissen, E., Saripalli, S., Arrowsmith, J R., McGarey, P., Scharer, K., Williams, P., and Blisniuk, K., in review. Rapid mapping of ultra-fine fault zone topography with Structure from Motion, submitted to *Geosphere*, December 2013.

### **Conference abstracts**

Johnson, K., Nissen, E., Arrowsmith, J R., Saripalli, S., McGarey, P., Scharer, K., and Williams, P. (2013). Rapid, decimeter-resolution fault zone topography from Structure-from-Motion (SfM), *SCEC Annual Meeting*.

Johnson, K., Nissen, E., Arrowsmith, J R., Saripalli, S., McGarey, P., Scharer, K., and Williams, P. (2013). Rapid, decimeter-resolution fault zone topography mapped with Structure-from-Motion, *AGU Fall Meeting*, G33A-0965.

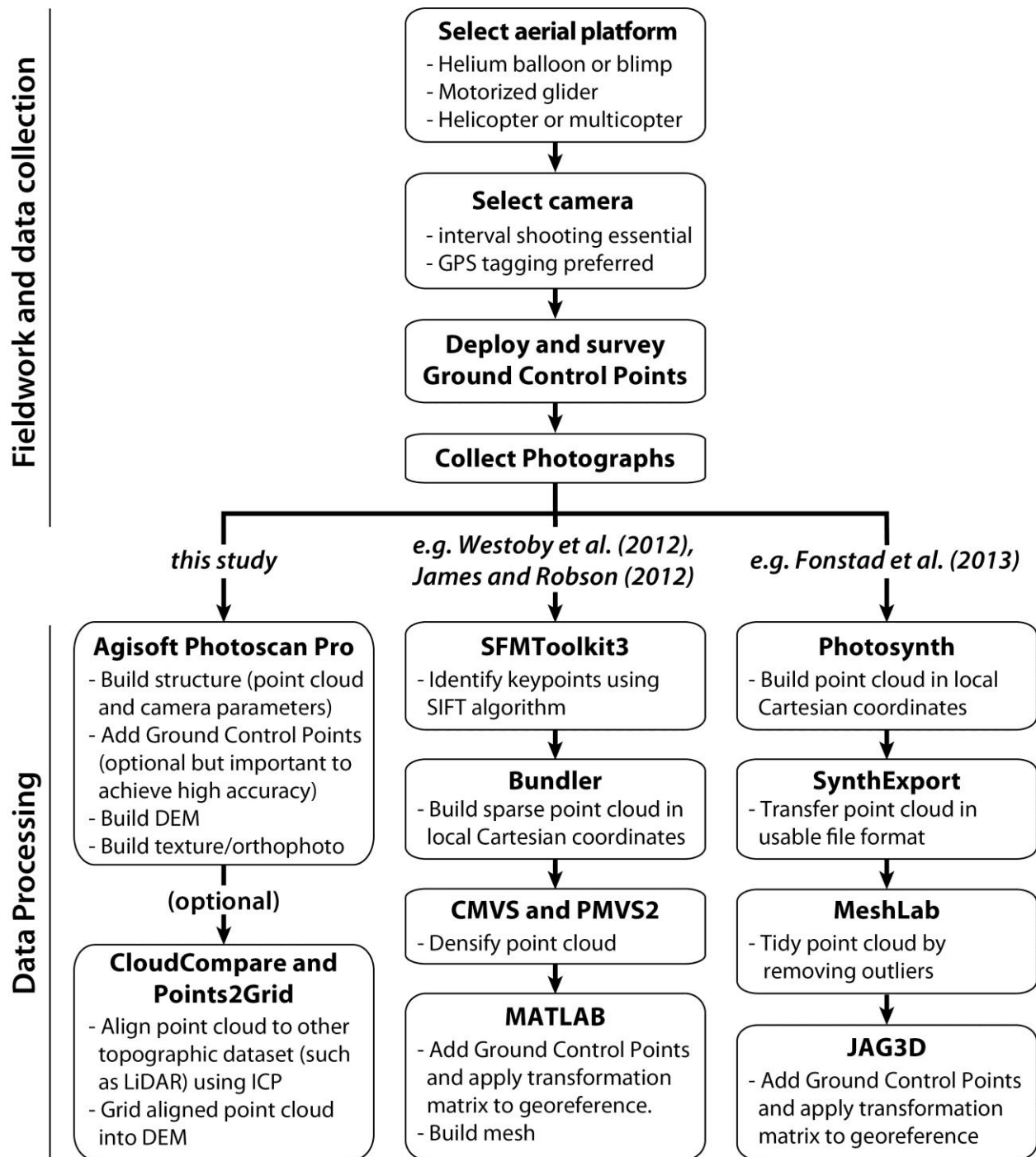


Figure 1. A summary of the workflow presented in this paper, including fieldwork and data collection (top) and data processing (bottom). In the lower part of the figure, our workflow is shown on the left and two alternative, published procedures are shown to the right.



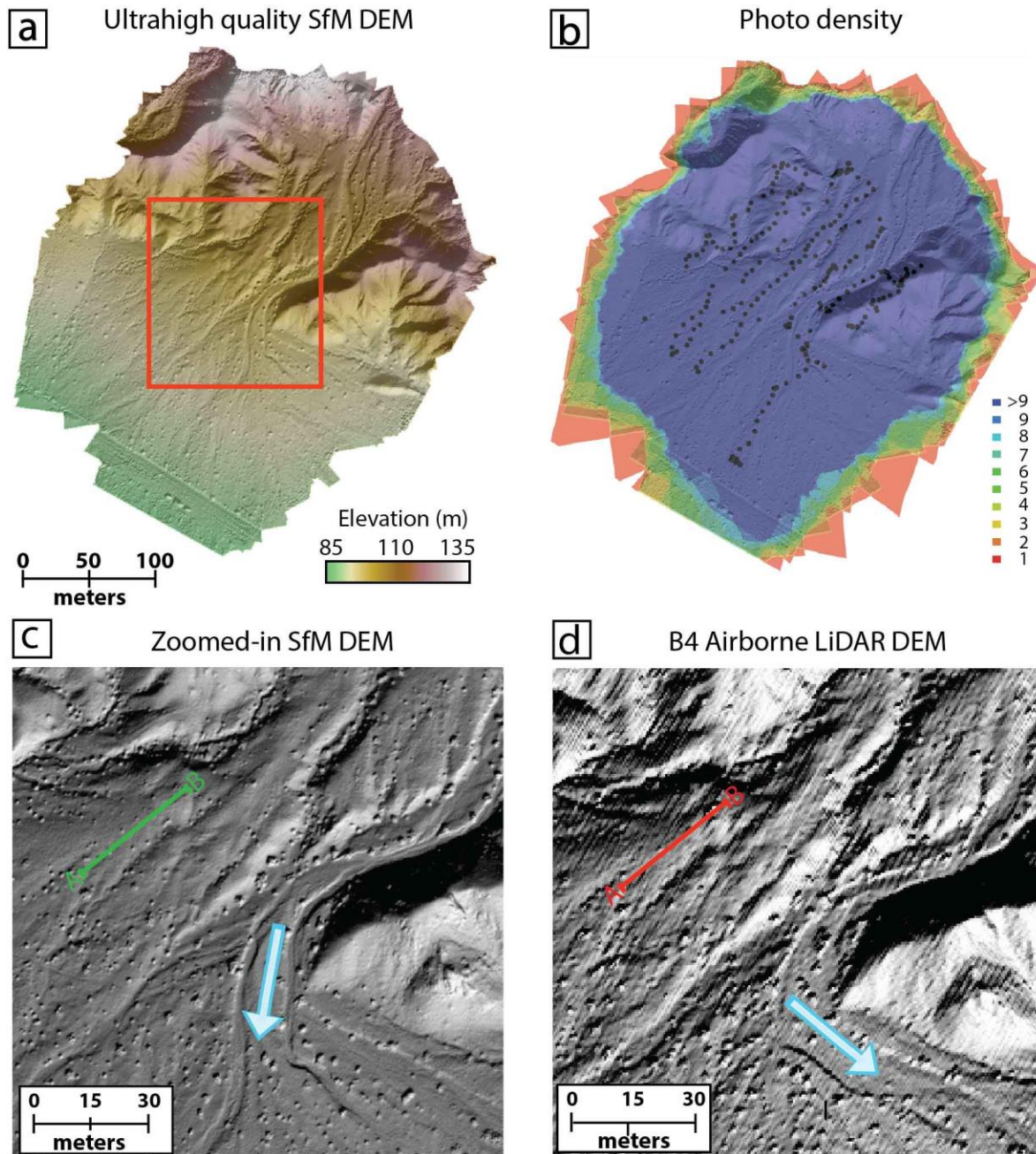


Figure 2. (a) Washington Street site SfM DEM produced with the photoset collected by the helium balloon at 50 m above ground level, artificially illuminated from azimuth 155°, elevation 21°. (b) Density map of photograph footprints for the same survey. Black dots show the camera location at the time of each photo. (c) Boxed region of SfM DEM shown in (a). The blue arrow shows path of the main channel in 2013. (d) B4 airborne LiDAR DEM over the same area. The DEM was generated from the raw point cloud using GEON points2grid, taking the inverse distance weighted value at 0.5 m node spacing and using a search radius of 0.8 m. Note the difference in channel flowpath when the LiDAR dataset was acquired in 2005 (blue arrow).

Absolute vertical distances (meters)  
from each LiDAR point to nearest SfM point

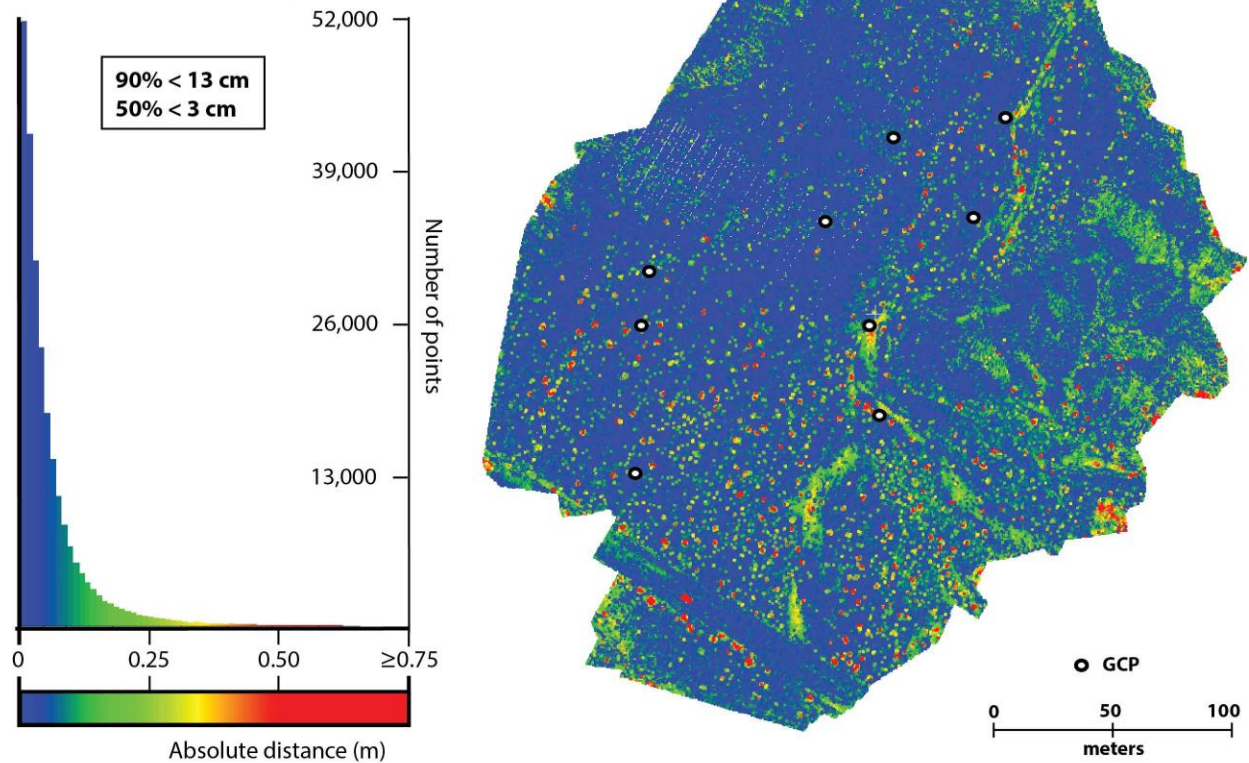


Figure 3. Comparison between LiDAR and the SfM dataset that was optimized with GCPs. (a) A map of the vertical distances between each LiDAR point and its closest SfM neighbor for the Washington Street site, and (b) a histogram showing the spread in these values across the entire scene. White dots indicate locations of the GCPs that were used. The color scale is the same in both map and histogram, and saturates at 0.5 m to better capture the variation at small distances. The comparison reveals that most of these distances are less than 3 cm. The worst locations occur at the perimeter of the scene, further from the GCPs and where topography was more rugged. The comparison also highlights some morphological changes in the scene: the red and yellow areas in the main channel probably represent the switching of the active channel between B4 surveying in 2005 and SfM mapping in 2013.